1 # **Volcano Tsunamis and their effects on moored vessels**
2 # **safety: The 2022 Tonga event**

3  Sergio Padilla[1], Íñigo Aniel-Quiroga[1], Rachid Omira[2,4], Mauricio González[1], Jihwan

4  Kim[2], Maria A. Baptista[3,4]

5  [1] Environmental Hydraulics Institute, Universidad de Cantabria (IHCANTABRIA), Avda. Isabel Torres,

6  15, Santander, Spain

7  [2] Instituto Português do Mar e da Atmosfera (IPMA), Lisbon, Portugal

8  3 Instituto Superior de Engenharia de Lisboa; Lisbon, Portugal

9  4 Instituto Dom Luiz, Faculdade de Ciências da Universidade de Lisboa

10  *Correspondence to*: Sergio Padilla (sergio.padilla@unican.es)

11  **Abstract.** The violent explosion of the Hunga Tonga-Hunga Ha'apai volcano on January 15, 2022, was the

12  origin of an atmospheric wave and a volcano-meteorological tsunami (VMT), both of which were recorded

13  worldwide. The Tonga tsunami event caused resonance effects, leading to wave amplification in some far-

14  field coastal areas like La Pampilla port in Callao, Peru, 10,000 km away from the volcano, where the

15  rupture of the Vessel mooring lines occurred 15 hours after the eruption, resulting the spill of over 11,000

16  barrels of crude oil. This study aims to better understand the coastal effects of the Tonga tsunami, focusing

17  on mooring loads in marine port environments. We examine how the VMT affected the safety of vessel

18  moorings, hypothesising that atmosphere-induced acoustic ocean waves exerted hydrodynamic loading that

19  endangered ships in port areas. A tsunami propagation obtained with a validated Boussinesq model at the

20  local scale in Callao Bay provides the input to the mooring system model applied to a vessel with similar

21  characteristics to the one docked at La Pampilla Port on the day of the Tonga event. This allows to study

22  the effect of the VMT on overstressing and the potential mooring breakage. The results suggest that the

23  Tonga tsunami event could be responsible for the movement and loss of positioning of the vessel.

24  Furthermore, atmospheric waves significantly increased mooring stresses, particularly on the starboard

25  quarter moorings. This event showed the need to prepare Tsunami Early Warning Systems and port

26  authorities for detecting and managing VMTs induced by atmospheric acoustic waves. The work provides

27  new insights into the far-field effects of the Tonga 2022 tsunami and discusses the lessons learned from

28  such an uncommon event.

29  ## 1.  Introduction

30  Volcanic activity can trigger tsunamis through underwater explosion, caldera collapse, pyroclastic flow,

31  flank collapse, or atmospheric gravity waves produced by large explosions (Paris, 2015). Throughout

32  history, tsunamis of volcanic origin have been poorly studied due to their scarcity, leading to a limited

33  understanding of their generation mechanisms and impacts at local, regional, and global scales (Hayward

34  et al., 2022). To better understand this type of tsunami geneses and, therefore, reduce the epistemic

...

35    uncertainties associated with it, several studies have been carried out (Antonopoulos, 1992; Pararas-

36    Carayannis, 1992, 2004), which also include aquatic environments other than oceans, such as great lakes

37    in Russia and The Philippines (Belousov et al., 2000; Falvard et al., 2018). In these studies, the 1883

38    eruption of the Krakatau volcano in the Sunda Strait (Indonesia), is commonly accepted as a main reference

39    and a unique example (Kienle et al., 1987), as it was the first event of its kind recorded by different

40    instruments worldwide (Paris et al., 2014; Yokoyama, 1981).

41    The Hunga Tonga-Hunga Ha'apai volcano (HTHH) is a submarine volcano near an island with the same

42    name, and located 65 km NNW of the island of Tongatapu capital of Tonga, Nukuʻalofa (20.55°S,

43    175.39°W, see location in Figure 1). It is one of several active volcanoes in the Kingdom of Tonga, an

44    archipelago nation in the South Pacific. The latest eruptive phase of the HTHH volcano began in mid-

45    December 2021 with vigorous shallow-water explosive activity. On January 15, 2022, the volcano erupted

46    at 4:00 a.m. UTC (Tonga Volcanic Eruption & Tsunami, 2022). Tonga experienced a volcano-

47    meteorological tsunami (VMT) following a violent volcanic explosion that generated atmospheric gravity

48    waves that propagated several times across the globe (Omira et al., 2022; Wright et al., 2022). These waves

49    resulted from particle agitation in the atmosphere, travelling both vertically and horizontally at sonic and

50    supersonic speeds (Kubota et al., 2022; Matoza et al., 2022; Wright et al., 2022; Dogan et al., 2023). Reports

51    of ocean-free surface elevations greater than 1 m, causing damage to ports and infrastructure, emerged after

52    the volcano explosion, originating from coastal areas near Tonga to the northwest and southeast Pacific

53    (Ramírez-Herrera et al., 2022; Imamura et al., 2022). The affected locations include Australia, New

54    Zealand, the United States, Mexico, and Peru, resulting in economic losses of approximately $102 million

55    due to damages to floating docks, vessels, and infrastructure (Terry et al., 2022; World Bank, 2024).

56    The Tonga VMT was exceptional as it travelled at faster speeds than common tsunamis, had a global reach,

57    affected the far-field coasts, and caused noticeable damages, human fatalities, and coastal hydrodynamic

58    effects (Terry et al., 2022; Omira et al., 2022; Lynett et al., 2022). In their study, Omira et al. (2022)

59    demonstrated that the primary source of the globally observed Tonga tsunami was the acoustic gravity

60    waves radiated from the volcanic explosion. Here, the sizeable tsunami at some distant coasts (i.e., South

61    America and Japan) was associated with the amplified ocean waves under Proudman resonance (Proudman,

62    1929) when the atmospheric wave propagated over very deep water (i.e., oceanic trenches). Other triggering

63    mechanisms, including the submarine volcanic explosion, likely contributed to the generation of the locally

64    observed tsunami in the far-field (Lynett et al., 2022; Omira et al., 2022).

65    The consequences of harbour-intruding long waves on moored vessels have been investigated by numerous

66    studies (Ayca and Lynett, 2016, 2018, 2021; Kirby et al., 2022; Wilson et al., 2017). Seismic tsunamis often

67    cause damage to port environments, such as broken moorings, collisions, or subsidence due to the large

68    amount of momentum flux travelling within the harbour (Lynett et al., 2022; Ohgaki et al., 2008; Inoue et

69    al., 2001). This also applies to tsunamis induced by atmospheric disturbances, which, like the previous ones,

70    have caused damage to ships, moored vessels, and small bays (Imamura et al., 2022; Thomson et al., 2009).

71    It has been observed in these studies that strong currents, often accompanying long-period waves, increase

72    the probability of generating large catastrophes in harbours (Shigeki and Masayoshi, 2009; Sakakibara et

73 al., 2010; Zheng et al., 2022; Lynett et al., 2012). Likewise, based on DOFs (Degrees Of Freedom), some
74 authors such as López and Iglesias (2014) agree with the hypothesis that the motions in the vessel's
75 horizontal plane (named roll, heave, and yaw) are strongly correlated with the total tsunami wave energy,
76 with the currents being quite significant in ship sway response (Inoue et al., 2001). Furthermore, Ohgaki et
77 al. (2008) and Zheng et al. (2022) mention that tsunamis are usually closer to the natural period of a mooring
78 system (>80 sec), which makes these waves more prone to generate damage. Given the non-linearity of
79 physical processes, it is pertinent to perform specific studies focused on each situation, configuration, and
80 need (Zheng et al., 2022).

81 In La Pampilla Port in Peru, 10,000 km away from the Tonga volcano, the Italian-flagged oil tanker Mare
82 Doricum reported the breakage of their mooring lines, 15 hours after the explosion of the HTHH volcano.
83 The ship captain associated the breaking of the vessel's moorings with the abnormal waves in the sea, for
84 which no warning was issued (SPDA Actualidad Ambiental, 2024). The Peruvian National Tsunami
85 Warning System (CNAT) stated that the Tonga tsunami did not generate a tsunami on the Peruvian coast
86 (CNAT, 2022). However, the tide gauge located in Callao Bay recorded a sudden change in sea level
87 coincident with the time of the accident (Sea level station monitoring facility, 2022). This article addresses
88 the impact of the Tonga 2022 tsunami on vessels moored on the Peruvian coast. It uses both sea-level data
89 analysis and numerical modelling to improve the understanding of the damage caused by far-field Tonga
90 VMT, studying its influence on the safety of moored vessels.

91 **2.        Data and Methods**

92 Considering the complexity of the Tonga tsunami event, which likely involved multiple triggering volcanic
93 mechanisms, analysing waves measured by both oceanic and atmospheric instruments is highly important
94 (Wright et al., 2022). Firstly, we used the wavelet analysis to examine the composition of the signals
95 recorded by both tidal gauges and DART buoys. Secondly, we studied the hydrodynamic effects of the
96 Tonga tsunami in the far field, using tsunami numerical simulations (Boussinesq-type model) over high-
97 resolution bathymetric models. Thirdly, we developed an analytical model to assess the stresses due to
98 hydrodynamic loads on moored vessels.

99 **2.1.        Air pressure and sea level data**

100 The data used in this study includes records from DART buoys, tide gauges, and weather stations in the
101 Pacific Ocean. Figure 1 shows the location of the instruments considered in this study, with red circles
102 representing the atmospheric pressure sensors, light blue triangles for the tide gauges, and yellow dots for
103 the DART buoys.

104 The deep-water sea level time series (**D1**, **D2**, and **D3**) were obtained from the DART buoys, which in turn
105 managed by the Center for Operational Oceanographic Products and Services of the National Oceanic and
106 Atmospheric Administration (NOAA, https://www.ndbc.noaa.gov/). Coastal sea level data used in this
107 study come from tidal stations connected in real-time to the Sea Level Station Monitoring Facility of
108 UNESCO's        Intergovernmental        Oceanographic        Commission        (IOC,        http://www.ioc-

109    sealevelmonitoring.org/). The **B1** air pressure data have been obtained from local agents in New Zealand
110    (NIWA, https://niwa.co.nz/) and those from stations **B3**, **B4**, **B5,** and **B8** came from the Dirección General
111    De Aeronáutica Civil de Chile (DGAC, https://climatologia.meteochile.gob.cl/) through the Chilean
112    Meteorological Office.

113
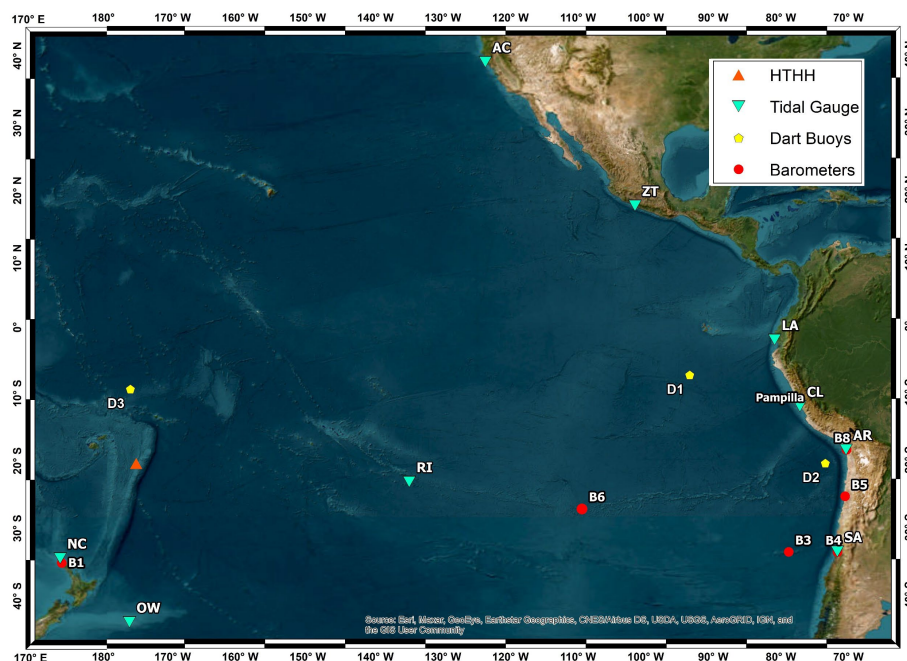
**Figure 1. Locations of the measuring instruments. Red circles show the atmospheric pressure sensors, the light blue triangles show the tide gauges, and the yellow circles refer to the Dart Buoys. The location of the Tonga volcano (HTHH) is the orange triangle.**

117    The sea level time series were de-tided using bandpass filters of 1.5 min-2.5 hours and 2 min - 3 hours for

118    DART and tide gauge data, respectively, following Lynett et al. (2022). For atmospheric pressure data, a

119    bandpass filter of 1.5 min - 2.5 hours was used (Table 1). Figure 2 shows the filtered time-series. The air-

120    pressure time-series shows a notable peak of approximately 2 hPa with the "N-wave" pulse shape associated

121    with the leading Lamb wave (Lynett et al., 2022; Omira et al., 2022).

| Type | ID | Name | Source (country) | Latitude (deg) | Longitude (deg) | Distance from source (km) | Sample (min) |
|---|---|---|---|---|---|---|---|
| Barometric | B1 | Nort Cape B. | New Zealand Gov | -35.134 | 173.263 | 1750 | 10 |
| | B3 | 330031 | Chilelan Gov. | -33.636 | -78.833 | 9110 | 1 |
| | B4 | 330030 | Chilelan Gov. | -33.656 | -71.613 | 9720 | 1 |
| | B5 | 250005 | Chilelan Gov. | -25.411 | -70.484 | 10230 | 1 |
| | B6 | 270001 | Chilelan Gov | -35.134 | 173.263 | 6530 | 1 |
| | B8 | 180042 | Chilelan Gov. | -18.513 | -70.266 | 10600 | 1 |

| | | | | | | | |
|---|---|---|---|---|---|---|---|
| Tide Gauge | NC | North Cape T.G. | IOC (New Zealand) | -34.410 | 173.050 | 1715 | 1 |
| | RI | Rikitea | IOC (France) | -23.118 | -134.969 | 4025 | 1 |
| | AC | Arena Cove | IOC (USA) | 38.913 | -123.705 | 8700 | 1 |
| | ZT | Zihuatanejo | IOC (Mexico) | 17.637 | -101.558 | 9155 | 1 |
| | GL | Galapagos | IOC (Ecuador) | -0.752 | -90.307 | 9410 | 1 |
| | SA | San Antonio | IOC (Chile) | -33.582 | -71.618 | 9720 | 1 |
| | OW | Owenga | IOC (New Zealand) | -44.025 | -176.369 | 2290 | 1 |
| | AR | Arica | IOC (Chile) | -18.476 | -70.323 | 10595 | 1 |
| | CL | Callao | IOC (Perú) | -12.069 | -77.167 | 10240 | 1 |
| | LA | La Libertad | IOC (Ecuador) | 13.485 | -89.319 | 10305 | 1 |
| DART | D1 | 32413 | NDBC (USA) | -7.421 | -93.484 | 8800 | 15 |
| | D2 | 32401 | NDBC (USA) | -20.474 | -73.421 | 10205 | 15 |
| | D3 | 51425 | NDBC (USA) | -9.511 | -176.258 | 1530 | 15 |

122     **Table 1. Description of measuring instruments.**

123
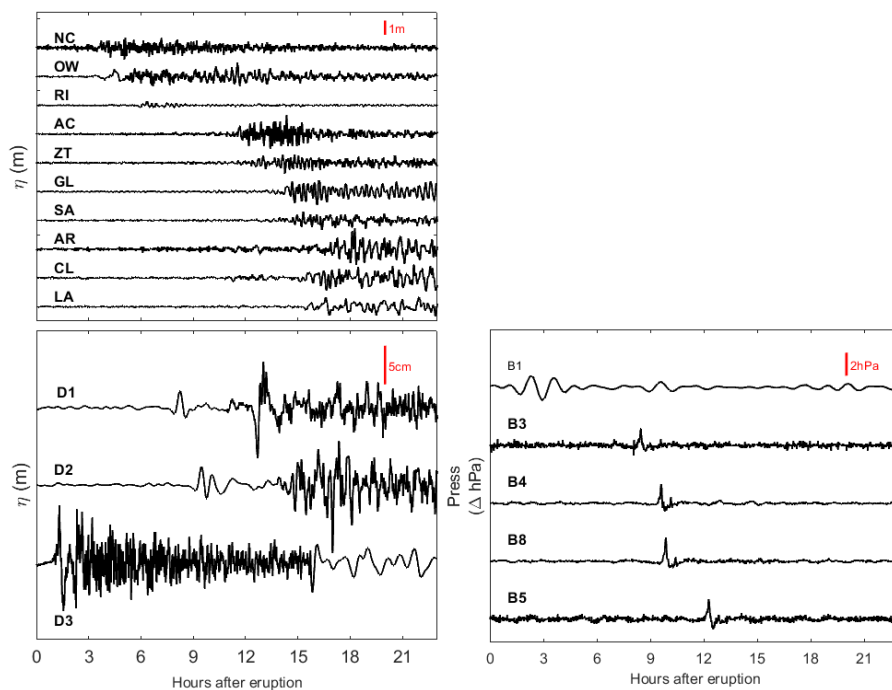
124

125     **Figure 2. De-tided time series. Air pressure data (right panel), tide gauge, and Dart data (left panel). Vertical**
126     **red lines used to scale the magnitude of the variations in each instrument.**

### 2.2. Spectral analysis

Spectral analysis is a practical tool for identifying the characteristic frequencies and energy levels in a time-series, particularly when it is composed of the superposition of signals with different frequencies. This method has found extensive application in the study of tsunamis (Abe, 2011; Rabinovich, 1997; Shevchenko et al., 2011; Satake et al., 2013; Baptista et al., 2016; Xu et al., 2022). In the time domain, we use wavelets to perform spectral analysis, allowing the estimation of the evolution of the spectral energy and, consequently, the first instants of energy increase for a given specific period.

### 2.3. Tsunami propagation model

Although air-ocean interaction has been recognized as a primary mechanism for the global fast-travelling Tonga 2022 tsunami (Omira et al., 2022), volcano-ocean interaction provided valid explanations for the near-field observation (Lynett et al., 2022; Pakoksung et al., 2022). As our primary target is Callao Bay, located approximately 10,000 km away from the HTHH volcano (Figure 3), we only focused on the tsunami induced by the atmospheric disturbances that followed the volcano explosion. The hypothesis of a point-source tsunami reaching the South American coast was ruled out considering the modelling results of a tsunami generated by the underwater explosion of the HTHH volcano (Omira et al., 2022).
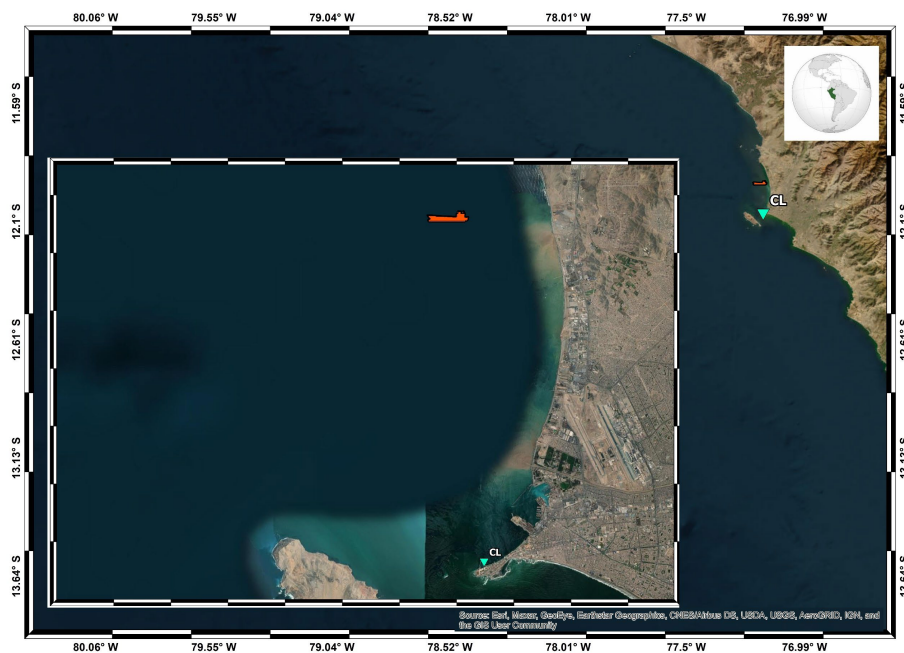
**Figure 3. Callao Bay and location of the vessel (Orange vessel) in the offshore port of La Pampilla, Peru.**

To simulate the VMT triggered by the explosion of the HTHH volcano, we used the finite volume GeoClaw code equipped with atmospheric pressure forcing terms that are handled using the flux-splitting method in momentum balance (Mandli and Dawson, 2014). This numerical code was validated in various

147  meteotsunami studies (Kim and Omira, 2021; Kim et al., 2022; Omira et al., 2022). The determination of

148  atmospheric source terms is based on barometric records from three distinct-selected observations in **B1**,

149  **B6,** and **B8** (see Table 1 for details). We assumed the symmetrical propagation of atmospheric pressure

150  from the source (HTHH volcano) at a constant speed of 310 m/s. Since a point source simulation on a

151  sphere has two singularities (at the origin and antipode), we used a relaxation method as described in Omira

152  et al. (2022).

153  Initially, our computational domain is between 40°S to 40°N and 170°E to 65°W, with a coarse bathymetry

154  resolution of 1 degree, as obtained from GEBCO (https://www.gebco.net/). To achieve a finer spatial

155  representation of the study area (i.e., Callao Bay), we employed four levels of refinement with resolutions

156  of 1°, 1°/5, 1°/30, and 1°/2, using an adaptive mesh refinement (AMR), with a maximum refinement level

157  of 3 across the entire domain. The full resolution of approximately 800 meters was reinforced near Callao

158  Bay with local higher-resolution bathymetry data (GEOGPS PERÚ, https://www.geogpsperu.com/). To

159  account for the bottom friction, GeoClaw software uses Manning's formulation, and the Manning

160  coefficient of 0.02 was considered in this work. Our simulations were conducted using the Madsen's

161  Boussinesq-type equations, with a constant value of B = 1/15 (Kim et al., 2017; Madsen and Sørensen,

162  1992).

163  The computation was performed on Intel Core i7-8700 CPU 3.2GHz using 10 cores corresponding to 1161

164  hours of propagation time, and 119 hours of wall time.

165  **2.4.    Stresses in moored ships model**

166  Here, we use an analytical model to estimate the loads on a vessel's mooring system under the

167  hydrodynamic effects of a tsunami (Tahar and Kim, 2004; OCIMF, 2010). The vessel is modelled as a rigid

168  body with six degrees of freedom (DOFs). The first three DOFs are the surge, sway, and heave ($x$, $y$, and $z$)

169  of the vessel's centre of gravity ($C_{OG}$), given in the global frame (Figure 4). The other three are the Euler

170  angles, roll, pitch, and yaw ($\alpha$, $\beta$, and $\gamma$), which describe the local frame rotation status with respect to the

171  global frame.

172  We considered two reference frames, the first of which is a global orthogonal inertial frame (fixed) with its

173  origin located somewhere at the mean water level, where the X-axis points eastward and the Z-axis points

174  upward for the global frame. The second is an orthogonal non-inertial frame, moving with the vessel, with

175  its origin located at the $C_{OG}$. The X-axis points toward the bow while the Z-axis points upward for the local

176  frame. The roll and pitch initial equilibrium positions are considered at zero degrees.

177

178
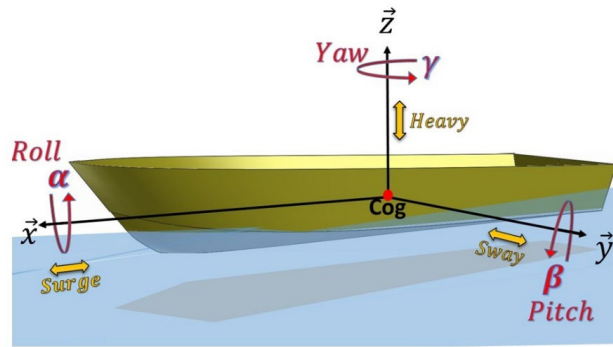
**Figure 4. Definition of Ship Motions in Six Degrees of Freedom, the yellow ones describe translation and the red**
179
**ones rotation.**
180

181 The model contemplates the vessel's hydromechanics and physics characteristics such as hydrostatic

182 stiffness (which considers both buoyancy and gravity forces), vessel mass $(m)$, metacentric heights $(GM_{t,l})$,

183 and inertial forces defined by the vessel's moments of inertia around the principal axes $(I_{x,y,z})$ as well as

184 describing the vessel's stability (Journée and Massie, 2001). The vessel's dynamics are described with the

185 equations of a forced and damped mass-spring system which allows the following initial value problem

186 (Eq. 1):

187
$$\begin{cases} \dot{Y} = f(Y,t) = \begin{bmatrix} \dot{\xi} \\ \ddot{\xi} \end{bmatrix} = \begin{bmatrix} \dot{\xi} \\ M^{-1} \cdot [B \cdot \dot{\xi} + G \cdot (\xi - \xi_0(t)) + F_m(\xi) + F_d(\xi,t)] \end{bmatrix} \\ Y(t=0) = Y_0 \end{cases} \quad (1)$$

188 where $Y_0$ is the initial vessel state vector, containing the initial position and the speed of the vessel, $B$ is the

189 damping matrix, $G$ is the stiffness matrix, $\xi$ is defined as the stacking of all the DOFs, $\xi_0$ is the initial

190 equilibrium position, and $F_m$ and $F_d$ are the mooring system forces and the current drag forces (Figure 5).

191

192
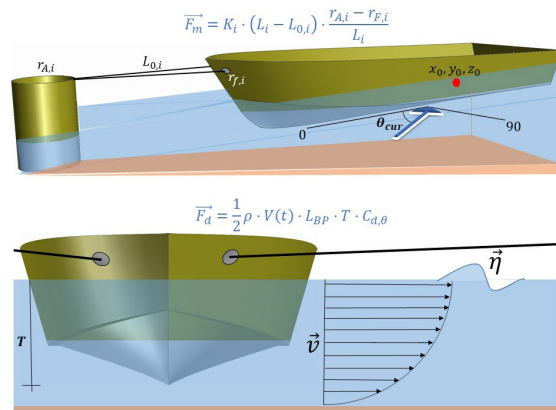
**Figure 5. Schematic layout of Ship Mooring system forces $F_m$ and Drag Forces $F_d$. The dynamics of the moored**
193
**vessel are defined with a second-order ordinary differential equation (ODE)**
194

195    The mooring system $\boldsymbol{F_m}$ is exclusively considered when the movement of the vessel results in a greater

196    increase in the length of the line $L_i$ compared to the previous position, as shown in the following Eq. (2):

197    $$F_{m,i} = \begin{cases} K_i \cdot (L_i - L_{0,i}) \cdot \frac{r_{A,i} - r_{F,i}}{L_i}, & L_i > L_{0,i} \\ 0, & L_i > L_{0,i} \end{cases} \qquad (2)$$

198    Where $K_i$ includes Elastic properties for the i-th line, $L_i$ is the line length, $r_A$ and $r_F$ are the pile and fairlead

199    positions (where the line is tied to the hull). The Morison drag force model (Oh et al., 2020) is utilized to

200    calculate the drag force $F_d$. The tsunami current at time $t$ is defined by its speed. The current drag force

201    changes depending on the angle of incidence, the $F_{d,x,y}$, calculated as Eq (3):

202    $$F_{d,x,y}(\xi, t) = \frac{1}{2} \rho \cdot V(t) \cdot L_{BP} \cdot T \cdot \begin{pmatrix} \cos(\gamma) & -\sin(\gamma) \\ \sin(\gamma) & \cos(\gamma) \end{pmatrix} \cdot \begin{pmatrix} C_x(|\theta(t)|) \\ C_y(|\theta(t)|) \cdot sgn(\theta(t)) \end{pmatrix} \qquad (3)$$

203    Where $C_x$ and $C_y$ are the drag forces in the $x$ and $y$ axes, $\rho$ is the water density, $V(t)$ is the tsunami current

204    velocity, $L_{BP}$ is the length between the perpendicular, T is the vessel's draft, and $\gamma$ is the Yaw DOF. We

205    considers the tsunami current angle $\theta$ to be parallel to the vessel's centerline at zero degrees. Finally, this

206    first-order ODE is integrated with a Runge-Kutta-4-5 method implemented in the SciPy Python library

207    (Dormand and Prince, 1980; Shampine, 1986).

208    The model inputs consist of the vessel's dimensions, hydromechanical and mass properties, the ship's

209    berthing scheme (including piles and fairleads coordinates), the line properties (such as young modulus and

210    length), and the temporal tsunami dynamics (including waves and currents time-series) at the vessel's

211    location. The model outputs the movements in each DOF and the resulting stress, measured in tons, for

212    each line throughout the time series.

213    **3.    Results**

214    **3.1.    Atmospheric and oceanic data analysis**

215    The analysis using wavelets is based on the hypothesis that the atmospheric waves' integral characteristics,

216    such as the periods and propagation velocities, remain reciprocal when resonance is generated between

217    atmospheric and oceanic waves. This allows the current knowledge extrapolation about atmospheric waves,

218    which have been extensively studied in the literature, and their effect on oceanic tsunami waves.

219    The results in Figure 6, Figure 7, and Figure 8 show the analysis of the recorded atmospheric and sea-level

220    signals, which are composed of three panels for each sensor. The top panel shows the filtered time-series

221    of both sea level and atmospheric pressure (blue and orange respectively). The orange arrow indicates the

222    leading Lamb wave arrival time respectively. The lower panel shows the spectral results (wavelets) of the

223    de-tided series of the ocean surface, the red-blue color scale marks the highest and lowest energy

224    concentrations respectively; to the right is the Fourier spectrum obtained from integrating the wavelet over

225    time.

226 Results in Figure 6 correspond to the tide gauges **NC**, **OW**, and **RI**, DART buoy **D3**, and pressure sensor

227 **B1** (see Figure 1 for location). Wavelets consistently show four energy groups for sensors tide gauges **NC,**

228 **OW, RI**, and DART buoy **D3**. These results allows for the identification of the initial characteristics of

229 tsunami waves forced by atmospheric waves, i.e., the arrival times and wave periods.

230

231
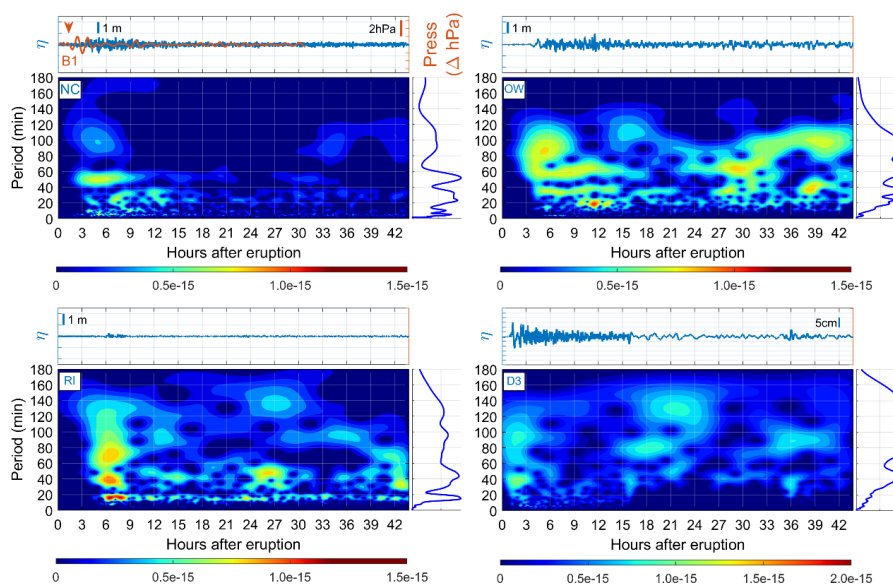
**Figure 6. Analysis of air-pressure and sea-level records at tide gauges NC (North Cape, New Zealand), OW (Owenga, New Zealand) and RI (Rikitea, France), DART buoy D3 (51425, NDBC), and air-pressure sensor B1 (North Cape, New Zealand). For each sensor, the time series of the air-pressure sensor (orange line) and tide gauge (blue line) are shown in the upper panel. The orange arrow refers to the arrival time of the leading pressure pulse. The panel to the right of the wavelet is the resulting frequency spectrum (FFT) of the time integration of the wavelet.**

238 The energy clusters fall within the 5-10 min, 20 to 40 min, 40 to 60 min, and 80-120 min periods, do the

239 energy clusters suggest that there were multiple mechanisms that generated the Tonga tsunami waves.

240 These results are consistent with the findings of previous studies (Hu et al., 2023; Kubota et al., 2022;

241 Omira et al., 2022). The manometer station **B1** and tide gauge **NC** allow the estimation of the propagation

242 velocities of the atmospheric disturbances as approximately 324 m/s.

243 Figure 7 shows far-field results (deep waters near the Peruvian coast) in sensors **D1-B3** and **D2-B5**. Air-

244 pressure time-series shows the 2 hPa pulse associated with the leading Lamb wave arrived first, followed

245 by second disturbances travelling at more than 200 m/s (Hu et al., 2022; Omira et al., 2022). DART buoy

246 wavelets provide more spectral information related to the physical properties of these atmospheric waves

247 coupled in the ocean. For example, DART Buoy **D2** shows that the first pulse coincides with the leading

248 Lamb wave between 30- and 60- minute periods arriving 9 hours after the main eruption. Then, there is a

249 group of energy contained in four ranges of periods: (i) about 10 min, (ii) between 20 and 40 min, (iii)

250 between 60 and 90, and (iv) between 100 and 140 min. The latter is possibly associated with the air-ocean

251    Proudman resonance that occurred on the Tonga Trench and propagated as common tsunami gravity waves

252    towards the Southern American coast (Omira et al., 2022).

253
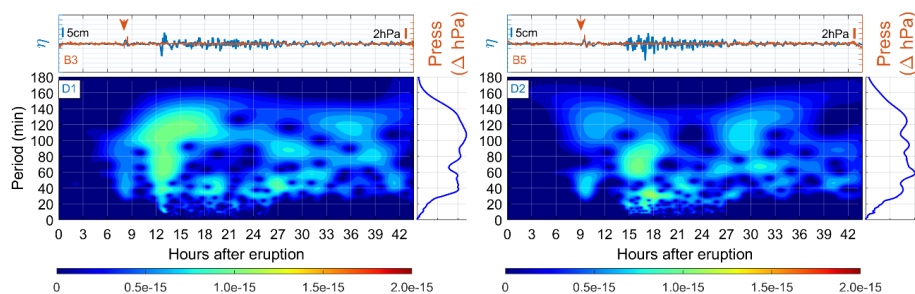
254

255    **Figure 7. Analysis of air-pressure and sea-level records at DART buoys D1 (32413, NDBC) and D2 (32401,**
256    **NDBC) and atmospheric pressure sensors B3 (330031, Chile) and B5 (250005, Chile). For each sensor, the**
257    **filtered time series of the atmospheric pressure sensor (orange line) and tide gauge (blue line) are shown in the**
258    **upper panel. The orange arrow refers to the arrival of the leading pressure pulse. The right panel of the wavelet**
259    **is the frequency spectrum resulting from the time integration of the wavelet.**

260    Figure 9 shows the spectral results for other locations along the Pacific American coasts. The South Pacific

261    American instruments are **SA-B4** (Chile), **AR-B8** (Chile), **CL-B5** (Peru) and **AL** (Ecuador). The sensors

262    in Central and North America are **ZT** (Mexico) and **AC** (USA). The wavelets' results in Chile, Mexico,

263    and the USA show several energy groups: one in 40 - 60 min periods, another group between 20 - 40 min,

264    and finally, energy in periods less than 10 min. Those wavelets exhibit a pattern similar to that observed in

265    deep water sensors, with a notable difference regarding the absence of periods close to 120 min.

266    Subsequently, Figure 8 shows the analysis for sensors **LA** (Ecuador), **CL-B5** (Peru), 15 km from the vessel

267    accident. The black dotted vertical line on the **CL** wavelet refers to the moment when the ship's moorings

268    break and the oil spill occurs, according to the captain of the ship Mare Doricum. It can be observed in the

269    **CL** wavelet that: (i) the Lamb wave coupled in the ocean (spectral energy between 30 - 60 min periods),

270    (ii) the mooring break moment coincides with the high period spectral energy (max between 110-130 min

271    period). Additionally, the energy within the 100 to 140 min period is present in deep water, (e.g., at DART

272    buoy **D1** in Figure 4) and amplified exclusively in front of the Ecuador and Peru coasts (**LA** and **CL** tide

273    gauges).

274
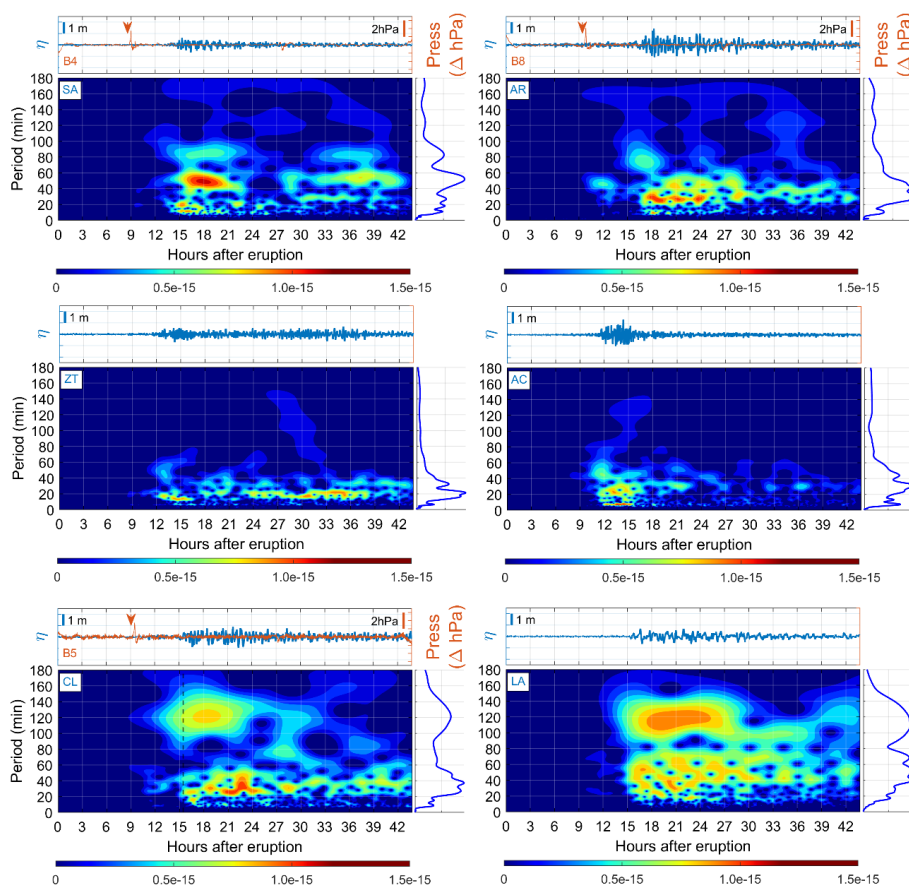
**Figure 8. Analysis of air-pressure and sea level records at the tide gauges of SA (San Antonio, Chile), AR (Arica, Chile), ZT (Zihuatanejo, Mexico), AC (California, USA), CL (Callao, Peru), and LA (La Libertad, Ecuador). The upper panel shows the time series of the atmospheric pressure sensor (orange line) and tide gauge (blue line). The orange arrow refers to the arrival of the leading Lamb wave. For the lower panel, we have the Wavelet. The vertical black dashed line in the CL wavelet refers to the instant when the vessel's moorings broke at La Pampilla port, Peru. The panel to the right of the wavelet is the frequency spectrum.**

## 3.2.    Numerical modelling of atmospheric pressure-induced tsunami waves

The numerical simulations have been calibrated/validated using both far- and near-field instrumental data. After validation, the significance of tsunami-like waves induced by atmospheric acoustic-gravity waves and tsunami-induced waves resulting from the submarine explosion were analyzed. We present the results in Figure 9, which shows the observed and simulated tsunami waveforms near the coast of Peru.

A comparison of observed and simulated tsunami waveforms at DART buoys (**D1** and **D2)** shows that the Boussinesq numerical model correctly reproduces the first tsunami wave. It also fairly reproduces the second train of tsunami waves, likely associated with air-ocean resonance in deep ocean (near Tonga trench), and travelling at common tsunami speeds (Omira et al., 2022; Hu et al., 2023; Kubota et al., 2022). In shallow waters, the model correctly reproduces the tide gauges **LA** and **CL** (closest to the port of La

292    Pampilla in Peru.), like in deep waters. It is interesting to note that the model succeeded in correctly

293    reproducing the 120-minute long-period wave (also observed in deep water).

294

295
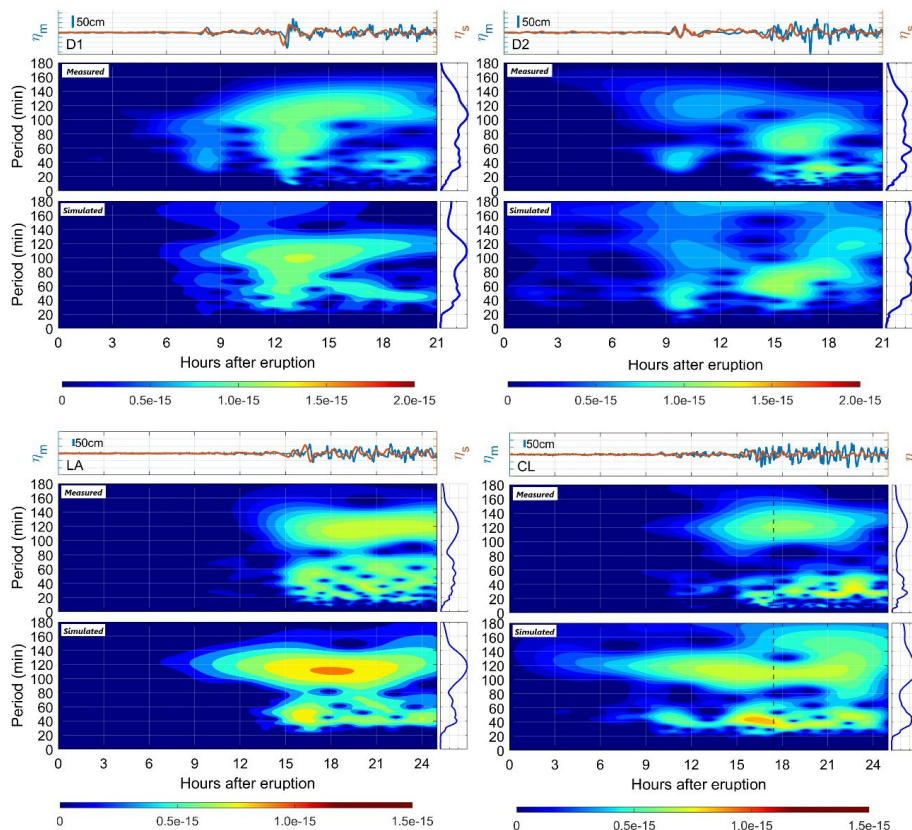
**Figure 9. Validation of numerical results at DART D1 and D2 buoys and tide gauges CL (Callao, Peru), and LA (La Libertad, Ecuador). For each buoy, the measured (blue line) and simulated (orange line) time series are shown in the upper panel. The lower panel shows the measured free sea surface wavelets (upper wavelet) and numerical simulation (lower wavelet). The vertical black dashed line in CL refers to the instant of the vessel mooring break in La Pampilla harbor, Peru. The panel to the right of each wavelet is the frequency spectrum.**

301    In general, an adequate VMT simulation is achieved, then the wavelets and Fourier transform show a correct

302    trend of the wave characteristics measured in each sensor, as shown in Figure 9. Wavelets corresponding

303    to both deep and shallow waters present several groups of waves forced by acoustic waves between 20-40

304    minutes, periods 40-60 min, and long-period waves about 120 min (Hu et al., 2023; Kubota et al., 2022;

305    Omira et al., 2022). Likewise, the Fourier spectra also show two distinguished groups of 40-60 min and

306    100-120 min in shallow water.

307    Compared to the DART buoys, the simulations exhibit similar behaviours because they are located at great

308    depths, where the influence of the bathymetry and the land boundaries is negligible. The simulations

309    demonstrate that tide gauges reveal variations such as earlier arrival times or more energy, possibly

310 associated with local effects and limitations in resolution. However, the model's results are similar to the

311 measured data.

312 Figure 10 displays simulation results for shallow water tide gauges **GL** and **SA** (located north and south of

313 Peru, respectively), demonstrating that the 120-minute period wave is exclusive of the coast of Peru and is

314 likely intensified by local effects. The wavelet analysis indicates that neither the simulated nor the measured

315 waves show a significant amplification of high-period energy, as seen in the sensors situated off the coast

316 of Peru.

317
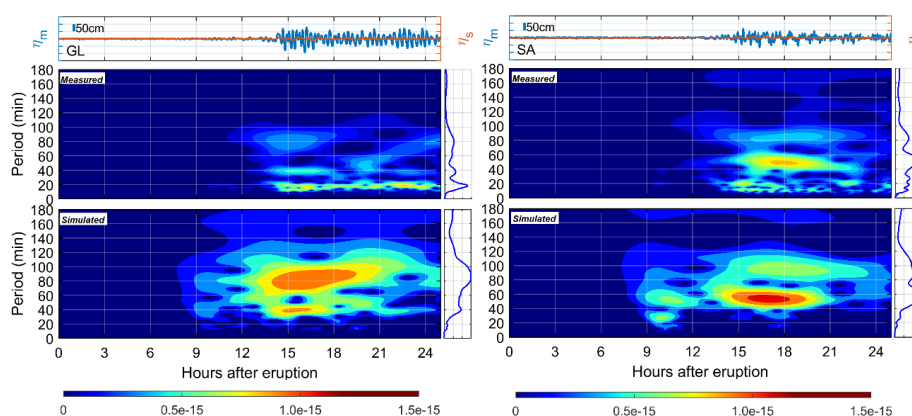
318

319 **Figure 10. Comparisons of the numerical results at the GL (Galapagos, Ecuador) and SA (San Antonio, Chile)**
320 **tide gauges are shown. For each tide gauge, the measured (blue line) and simulated (orange line) time series are**
321 **shown in the upper panel. The lower panel has measured (upper wavelet) and simulated (lower wavelet) ocean**
322 **results. The panel to the right of each wavelet is the frequency spectrum.**

323 **3.3.      Vessel response due to acoustic and tsunami waves**

324 The model described in Section 2.4 was implemented to estimate the mooring stresses due to tsunami

325 hydrodynamic effects produced during the Tonga event. The purpose is to demonstrate the variability in

326 stress levels when exposed to tsunami waves of varying periods and, therefore, different hydrodynamic

327 conditions.

328 The current velocity and water elevation time-series were extracted from the Boussinesq tsunami model,

329 presented in Section 2.3 and validated in Section 3.2 at coordinates 11º56' **S**,77º11' **W**, the location of

330 Terminal 2 of La Pampilla port (as shown in Figure 3). Figure 11 describes the mooring scheme. Each pile

331 is defined as immovable to focus stresses on every line. The scheme is similar to the one found in Terminal

332 2 of the Port of La Pampilla in Peru during the mooring-break accident.
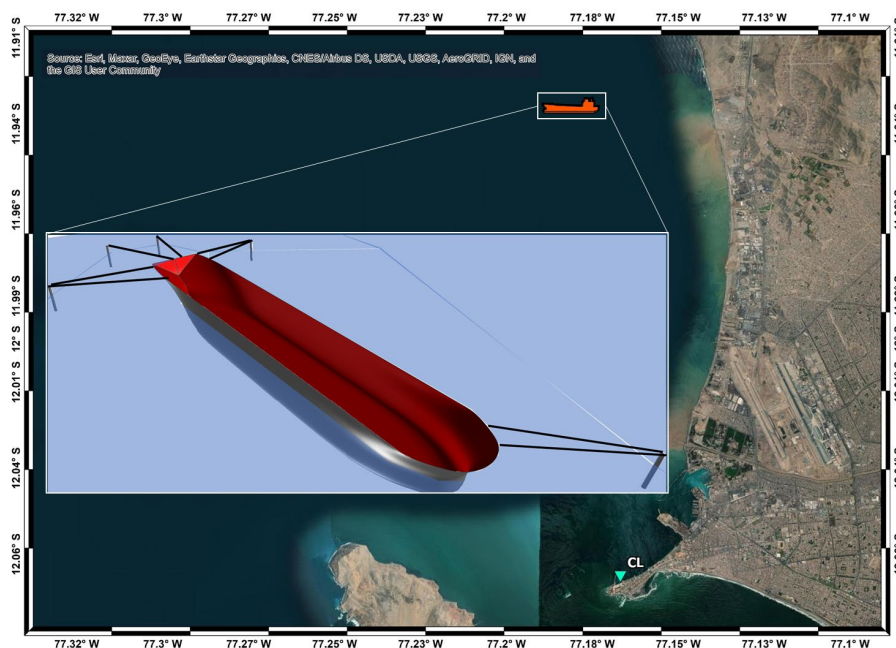
**Figure 11. La Pampilla port location (square in left map) and berthing scheme implemented in the mooring lines stress model (right panel).**

In Tables 2 and 3 presents the vessel's description and its hydromechanical characteristics. The entire mooring system schematic and the data used in the model are provided. The vessel used in this study is not the oil tanker Mare Doricum, but rather one with comparable physical characteristics. The vessel is moored to five buoys with eight moorings, one forward and four at the stern (in addition to two stern anchors anchored at a depth of 18 meters). The ship is considered fully loaded throughout the simulation. (Figure 12).

| | | |
|---|---:|---|
| LOA | 274 | m |
| Beam | 48 | m |
| draft | 8 | m |
| Mass | 119.311 | Ton |
| Xcg | 118.3 | m |
| Ycg | 0 | m |
| Zcg | -6.65 | m |
| Ixx | 21470000 | Ton m2 |
| Iyy | 515780000 | Ton m2 |
| Izz | 515780000 | Ton m2 |
| MGt | 20.042 | m |
| MGl | 471.824 | m |
| Displacement | 100,434 | Ton |

| Waterplane area | 9920.68 | m2 |
|---|---|---|
| Gz | 99949.56131 | Ton m |
| Groll | 2012895.542 | Ton m |
| Gpitch | 47387108.39 | Ton m |

342 **Table 2. Description of the vessel used in the mooring stress simulation**

343

| Line number | Pile position $r_{A,i}$ (m,m,m) | Fairlead position $r_{f,i}$ (m,m,m) | Length $L_{0,i}$ (m) |
|---|---|---|---|
| 0 | (208.27, 80.13, 3.00) | (138.34, 5.65, 6.00) | 103.21 |
| 1 | (208.27, 80.13, 3.00) | (121.00, 13.42, 6.00) | 115.78 |
| 2 | (-152.09, 96.13, 3.00) | (-85.20, 24.30, 6.00) | 105.64 |
| 3 | (-152.09, 96.13, 3.00) | (-92.13, 23.61, 6.00) | 103.54 |
| 4 | (-220.98, 25.94, 3.00) | (-118.19, 3.57, 6.00) | 107.30 |
| 5 | (-225.43, -57.61, 3.00) | (-117.98, -4.43, 6.00) | 125.63 |
| 6 | (-184.75, -120.44, 3.00) | (-89.22, -23.95, 6.00) | 136.73 |
| 7 | (-184.75, -120.44, 3.00) | (-82.04, -24.33, 6.00) | 142.59 |

344 **Table 3. Description of the mooring system used in the stress simulation**

345
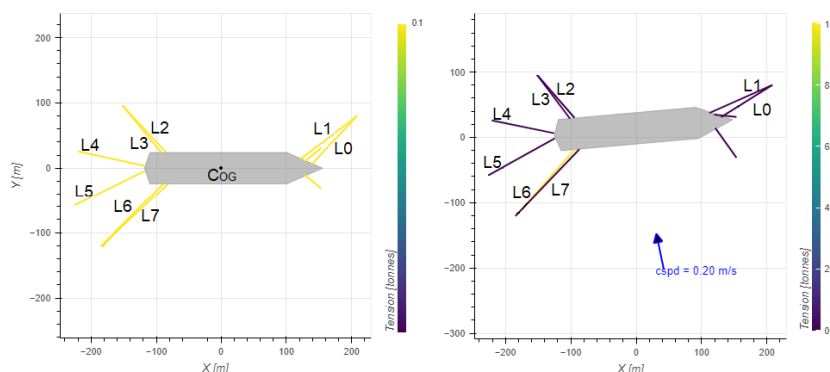
346
347 **Figure 12. On the left is the initial layout with the origin at the ship's C$_{OG}$ and on the right is the**
348 **moment of mooring breakage, where the yellow and purple colors mark the maximum and minimum stress**
349 **values, respectively.**

350 The results of the DOFs along the simulation are presented in Figure 13. The first instances of ship

351 movement occur about 9 to 10 hours after the volcano erupts, coinciding with the arrival of atmospheric

352 waves (VMT), with variations in the order of 2 m, 8 m, and 2 degrees for the DOFs Surge, Sway, and Yaw,

353 respectively, in the movements directly associated with tsunami hydrodynamic loads (López and Iglesias,

354 2014). Then, 15 hours after the eruption, when the 120-minute period wave is present and the mooring

355 breaks, further ship motion is generated, drastically increasing the vessel mentioned above DOFs values.

356 The model results indicate that the movement was caused by the VMT. The anchored ship aligns with the

357 surge, sway, and yaw; with a maximum deviation of 9 meters, 14 meters, and 5 degrees, respectively, which

358 is more than enough to produce the breakage of the mooring system according to the port authority of La

359 Pampilla (CPAAAAE, 2023).

360
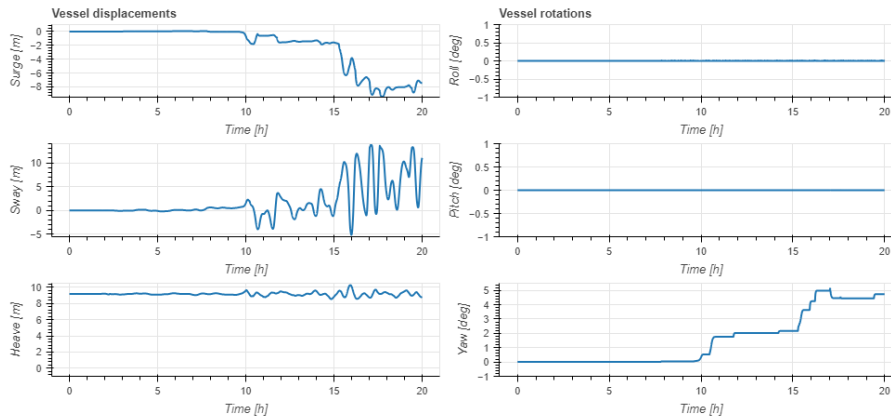
361

362 **Figure 13. Time series of ship 6 degrees of freedom obtained from numerical simulation. Measured in hours**
363 **after the eruption.**

364 To support the hypothesis that the 120-minute long-period wave along the Peruvian coast caused the
365 mooring to break, a comparison was made between the stresses obtained by forcing with the VMT time-
366 series and the tsunami caused only by the submarine explosion. The stress results for each line in both cases
367 are shown in Figure 14. This illustration shows two things. Firstly, with the VMT, the lines that are primarily
368 under stress are the starboard moorings lines number 0, 4, and 6, the latter having the maximum load (96
369 tons), which exceeds the Minimum Breaking Load (MBL) by more than 10 tons. The increase in stresses
370 was due to the configuration of the mooring layout, tsunami wave direction, and hydrodynamic effects,
371 which could cause the mooring line to break. Secondly, the findings suggest that the VMT results in a
372 significant increase in mooring stresses, exceeding 10-times the levels observed during the tsunami-only
373 event (where the VMT is not included in the simulation). These results confirm that the atmospheric waves
374 generated during the volcanic eruption have transmitted energy to the ocean, generating tsunami-like waves
375 that have affected the far field.
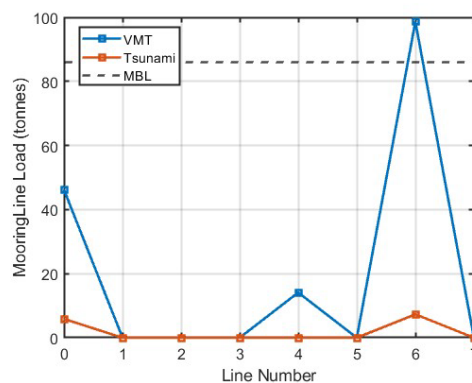
376

377 **Figure 14. Maximum stresses obtained from the simulation at each mooring. Blue and orange lines represent**
378 **the results of the simulations with and without atmospheric waves, respectively.**

379   **4.       Conclusions**

380   The propagation of atmospheric waves and their coupling with the ocean were extensively studied
381   following the Tonga event. Although epistemic uncertainties associated with the event are important, it was
382   possible to understand the main forcers and effects of the volcano-meteorological tsunami (VMT) in the
383   far-field, where the atmospheric waves were the dominant generation mechanism. The air-ocean Proudman
384   resonance in deep water was the driving mechanism that caused sizeable gravity waves, which had very
385   similar characteristics to those of a tectonic-source tsunami.

386   The potential of the explosion-induced atmospheric waves to magnify tsunamis once they pass over oceanic
387   regions of great depth has become apparent. This happened near the Tonga trench in the propagation
388   direction of South America (Figure 3-c in Omira et al., 2022), helping to understand the origin of long-
389   period tsunami waves propagated toward Peru. The spectral analysis results establish the influence of the
390   atmospheric waves generated by the HTHH volcano.

391   The presence of the high period waves exclusively in the tide gauges of Peru and Ecuador (**CL** and **LA,**
392   respectively) could be explained by several processes associated with shoaling. These processes could
393   include the width and slope of the continental shelf (which is wider on the Peruvian coast than on the
394   Chilean coast, for example) and the effects associated with topographic boundaries and their geometry,
395   such as the natural bay oscillation modes.

396   Considering that, the 120-minutes long-period waves were associated with the air-ocean-resonance of the
397   Tonga event and that numerical simulations additionally show the mooring line stress using the VMT time-
398   series, it is possible to conclude that the Tonga tsunami caused the overstressing and subsequent accident
399   in the port of La Pampilla, Peru.

400   Various processes, including hydrodynamic loads on the ship's hull, can threaten the stability of moored
401   vessels. These loads primarily affect the horizontal plane, which influences the sway, surge, and yaw
402   degrees of freedom. The VMT produced during the Tonga 2022 event was accompanied by long-period
403   waves and currents, which could affect the stability of the mooring system in the port of La Pampilla, Peru.

404   The hydrodynamic effects that these very long-period waves can cause in port environments can generate
405   damages similar to those of tectonic-source tsunamis, affecting infrastructure, vessels, and merchandise.
406   One unique characteristic of VMT events is that their waves do not dissipate energy with a ratio of $r^{-1/2}$
407   (where r is the distance from the generation origin). Instead, they can be amplified thousands of kilometers
408   away from their origin, presenting an increased threat to the stability of port environments in the far field.

409   **4.1.  Final Considerations**

410   Coastal and port infrastructure are not prepared to respond preventively to these Tonga-type tsunamis,
411   leaving them "unprotected", as tsunami warnings are not issued once a volcano eruption is known.
412   Furthermore, in the analyzed event, the initial ocean disturbance arrived earlier than anticipated because

413 the atmospheric waves produced a VMT that travelled at sonic velocity. This statement holds relevance as

414 state and international authorities are responsible for maritime safety and the creation of cautions-warnings

415 and suggestions to aid distinct users in coastal and offshore locations.

416 This event showed the need for Tsunami Early Warning Systems (TWS) to be prepared to include

417 atmospheric waves and detect them from existing monitoring sensors. In addition, Standard Operational

418 Procedures need to include protocols for these events to avoid damage to port facilities and ships, such as

419 the breaking of moorings and ship collisions. These events can also generate local flooding increasingly far

420 away from the origin and affect the population and coastal infrastructures (cities, nuclear reactors,

421 petrochemical industry, etc.). Therefore, efforts towards the incorporation of tsunamis caused by volcanic

422 acoustic waves in tsunami warning systems are needed.

423 **5. Author contribution**

424 Supervision and methodology (G.M and A-Q.I); Waves simulations (K.J and O.R); revision (B.M and O.R).

425 All authors have read and agreed to the published version of the manuscript.

426 **6. Competing interests**

427 At least one of the co-authors is a member of the editorial board of Natural Hazards and Earth System

428 Sciences.

429 **7. Acknowledgement**

430 This research was supported by an FPU (Formación de Profesorado Universitario) grant from the Spanish

431 Ministry of Science and Innovation (MCINN) to the first author. We have gratitude to The Ocean Energy

432 and Offshore Engineering Group of IHCANTABRIA for the model of mooring stresses. In addition, the

433 authors of this work would like to thank the various state institutions that have provided measured

434 atmospheric data mentioned in Chapter 2: IDEAM (Colombia), SENAMHI (Perú), DGAC (Chile), NIWA

435 (New Zealand), NOAA (USA) and IOC.

436 **8. References**

437 Abe, K.: Synthesis of a Tsunami Spectrum in a Semi-Enclosed Basin Using Its Background Spectrum, Pure

438 Appl. Geophys., 168, 1101–1112, https://doi.org/10.1007/s00024-010-0222-x, 2011.

439 Ana Baptista, M., Miguel Miranda, J., Batlló, J., Lisboa, F., Luis, J., and Maciá, R.: New study on the 1941

440 Gloria Fault earthquake and tsunami, Nat. Hazards Earth Syst. Sci., 16, 1967–1977,

441 https://doi.org/10.5194/nhess-16-1967-2016, 2016.

442 Antonopoulos, J.: The great Minoan eruption of Thera volcano and the ensuing tsunami in the Greek

443 Archipelago, Nat. Hazards, 5, 153–168, https://doi.org/10.1007/BF00127003, 1992.

444   Ayca, A. and Lynett, P. J.: Effect of tides and source location on nearshore tsunami-induced currents, J.
445   Geophys. Res. Ocean., 121, 8807–8820, https://doi.org/10.1002/2016JC012435, 2016.

446   Ayca, A. and Lynett, P. J.: DEBRIS AND VESSEL TRANSPORT DUE TO TSUNAMI CURRENTS IN
447   PORTS AND HARBORS, Coast. Eng. Proc., 68, https://doi.org/10.9753/icce.v36.currents.68, 2018.

448   Ayca, A. and Lynett, P. J.: Modeling the motion of large vessels due to tsunami-induced currents, Ocean
449   Eng., 236, 109487, https://doi.org/10.1016/j.oceaneng.2021.109487, 2021.

450   Belousov, A., Voight, B., Belousova, M., and Muravyev, Y.: Tsunamis generated by subaquatic volcanic
451   explosions: Unique data from 1996 Eruption in Karymskoye Lake, Kamchatka, Russia, Pure Appl.
452   Geophys., 157, 1135–1143, https://doi.org/10.1007/s000240050021, 2000.

453   CPAAAAE: Informe Final sobre las acciones de los funcionarios públicos y privados que ocasionaron el
454   derrame de petróleo de la Empresa Multinacional REPSOL YPF S.A., Lima, 421 pp., 2023.

455   Dogan, G. G., Yalciner, A. C., Annunziato, A., Yalciner, B., and Necmioglu, O.: Global propagation of air
456   pressure waves and consequent ocean waves due to the January 2022 Hunga Tonga-Hunga Ha'apai
457   eruption, Ocean Eng., 267, 113174, https://doi.org/10.1016/j.oceaneng.2022.113174, 2023.

458   Dormand, J. R. and Prince, P. J.: A family of embedded Runge-Kutta formulae, J. Comput. Appl. Math., 6,
459   19–26, https://doi.org/10.1016/0771-050X(80)90013-3, 1980.

460   Falvard, S., Paris, R., Belousova, M., Belousov, A., Giachetti, T., and Cuven, S.: Scenario of the 1996
461   volcanic tsunamis in Karymskoye Lake, Kamchatka, inferred from X-ray tomography of heavy minerals in
462   tsunami deposits, Mar. Geol., 396, 160–170, https://doi.org/10.1016/j.margeo.2017.04.011, 2018.

463   Hamilton, G. D.: National Data Buoy Center Programs, Bull. Am. Meteorol. Soc., 67, 411–415,
464   https://doi.org/10.1175/1520-0477(1986)067<0411:NDBCP>2.0.CO;2, 1986.

465   Hayward, M. W., Whittaker, C. N., Lane, E. M., Power, W. L., Popinet, S., and White, J. D. L. L.:
466   Multilayer modelling of waves generated by explosive subaqueous volcanism, Nat. Hazards Earth Syst.
467   Sci., 22, 617–637, https://doi.org/10.5194/nhess-22-617-2022, 2022.

468   Hu, G., Li, L., Ren, Z., and Zhang, K.: The characteristics of the 2022 Tonga volcanic tsunami in the Pacific
469   Ocean, Nat. Hazards Earth Syst. Sci., 23, 675–691, https://doi.org/10.5194/nhess-23-675-2023, 2023.

470   Hu, Y., Li, Z., Wang, L., Chen, B., Zhu, W., Zhang, S., Du, J., Zhang, X., Yang, J., Zhou, M., Liu, Z.,
471   Wang, S., Miao, C., Zhang, L., and Peng, J.: Rapid Interpretation and Analysis of the 2022 Eruption of
472   Hunga Tonga-Hunga Hàapai Volcano with Integrated Remote Sensing Techniques, Wuhan Daxue Xuebao
473   (Xinxi    Kexue    Ban)/Geomatics    Inf.    Sci.    Wuhan    Univ.    [J],    47,    242–251,
474   https://doi.org/10.13203/J.WHUGIS20220050, 2022.

475   Imamura, F., Suppasri, A., Arikawa, T., Koshimura, S., Satake, K., and Tanioka, Y.: Preliminary
476   Observations and Impact in Japan of the Tsunami Caused by the Tonga Volcanic Eruption on January 15,
477   2022, Pure Appl. Geophys., 179, 1549–1560, https://doi.org/10.1007/s00024-022-03058-0, 2022.

478   Inoue, Y., Rafiqul Islam, M., and Murai, M.: Effect of wind, current and non-linear second order drift forces
479   on a moored multi-body system in an irregular sea, in: Oceans Conference Record (IEEE), 1915–1922,
480   https://doi.org/10.1109/oceans.2001.968139, 2001.

481   Sea level station monitoring facility: https://www.ioc-sealevelmonitoring.org/station.php?code=call, last
482   access: 1 February 2022.

483   Journée, J. M. J. and Massie, W. W.: Offshore Hydromechanics, First Edition,

484 https://ocw.tudelft.nl/courses/offshore-hydromechanics/, 2001.

485 Kienle, J., Kowalik, Z., and Murty, T. S.: Tsunamis generated by eruptions from Mount St. Augustine

486 Volcano, Alaska, https://doi.org/10.1126/science.236.4807.1442, 1987.

487 Kim, J. and Omira, R.: The 6–7 July 2010 meteotsunami along the coast of Portugal: insights from data

488 analysis and numerical modelling, Nat. Hazards, 106, 1397–1419, https://doi.org/10.1007/s11069-020-

489 04335-8, 2021.

490 Kim, J., Pedersen, G. K., Løvholt, F., and LeVeque, R. J.: A Boussinesq type extension of the GeoClaw

491 model - a study of wave breaking phenomena applying dispersive long wave models, Coast. Eng., 122, 75–

492 86, https://doi.org/10.1016/j.coastaleng.2017.01.005, 2017.

493 Kim, J., Choi, B. J., and Omira, R.: On the Greenspan resurgence of meteotsunamis in the Yellow Sea—

494 insights from the newly discovered 11–12 June 2009 event, Nat. Hazards, 114, 1323–1340,

495 https://doi.org/10.1007/s11069-022-05427-3, 2022.

496 Kirby, J. T., Grilli, S. T., Horrillo, J., Liu, P. L.-F., Nicolsky, D., Abadie, S., Ataie-Ashtiani, B., Castro, M.

497 J., Clous, L., Escalante, C., Fine, I., González-Vida, J. M., Løvholt, F., Lynett, P., Ma, G., Macías, J.,

498 Ortega, S., Shi, F., Yavari-Ramshe, S., and Zhang, C.: Validation and inter-comparison of models for

499 landslide tsunami generation, Ocean Model., 170, 101943, https://doi.org/10.1016/j.ocemod.2021.101943,

500 2022.

501 Kubota, T., Saito, T., and Nishida, K.: Global fast-traveling tsunamis driven by atmospheric Lamb waves

502 on the 2022 Tonga eruption, Science (80-. )., 377, 91–94, https://doi.org/10.1126/science.abo4364, 2022.

503 López, M. and Iglesias, G.: Long wave effects on a vessel at berth, Appl. Ocean Res., 47, 63–72,

504 https://doi.org/10.1016/j.apor.2014.03.008, 2014.

505 Lynett, P., McCann, M., Zhou, Z., Renteria, W., Borrero, J., Greer, D., Fa'anunu, O., Bosserelle, C., Jaffe,

506 B., La Selle, S. P., Ritchie, A., Snyder, A., Nasr, B., Bott, J., Graehl, N., Synolakis, C., Ebrahimi, B., and

507 Cinar, G. E.: Diverse tsunamigenesis triggered by the Hunga Tonga-Hunga Ha'apai eruption, Nature, 609,

508 728–733, https://doi.org/10.1038/s41586-022-05170-6, 2022.

509 Lynett, P. J., Borrero, J. C., Weiss, R., Son, S., Greer, D., and Renteria, W.: Observations and modeling of

510 tsunami-induced currents in ports and harbors, Earth Planet. Sci. Lett., 327–328, 68–74,

511 https://doi.org/10.1016/j.epsl.2012.02.002, 2012.

512 Madsen, P. A. and Sørensen, O. R.: A new form of the Boussinesq equations with improved linear

513 dispersion characteristics. Part 2. A slowly-varying bathymetry, Coast. Eng., 18, 183–204,

514 https://doi.org/10.1016/0378-3839(92)90019-Q, 1992.

515 Mandli, K. T. and Dawson, C. N.: Adaptive Mesh Refinement for Storm Surge, Ocean Model., 75, 36–50,

516 https://doi.org/10.1016/j.ocemod.2014.01.002, 2014.

517 Matoza, R. S., Fee, D., Assink, J. D., Iezzi, A. M., Green, D. N., Kim, K., Toney, L., Lecocq, T.,

518 Krishnamoorthy, S., Lalande, J. M., Nishida, K., Gee, K. L., Haney, M. M., Ortiz, H. D., Brissaud, Q.,

519 Martire, L., Rolland, L., Vergados, P., Nippress, A., Park, J., Shani-Kadmiel, S., Witsil, A., Arrowsmith,

520 S., Caudron, C., Watada, S., Perttu, A. B., Taisne, B., Mialle, P., Le Pichon, A., Vergoz, J., Hupe, P., Blom,

521 P. S., Waxler, R., De Angelis, S., Snively, J. B., Ringler, A. T., Anthony, R. E., Jolly, A. D., Kilgour, G.,

522 Averbuch, G., Ripepe, M., Ichihara, M., Arciniega-Ceballos, A., Astafyeva, E., Ceranna, L., Cevuard, S.,

523 Che, I. Y., De Negri, R., Ebeling, C. W., Evers, L. G., Franco-Marin, L. E., Gabrielson, T. B., Hafner, K.,

524 Harrison, R. G., Komjathy, A., Lacanna, G., Lyons, J., Macpherson, K. A., Marchetti, E., McKee, K. F.,

525 Mellors, R. J., Mendo-Pérez, G., Mikesell, T. D., Munaibari, E., Oyola-Merced, M., Park, I., Pilger, C.,

526 Ramos, C., Ruiz, M. C., Sabatini, R., Schwaiger, H. F., Tailpied, D., Talmadge, C., Vidot, J., Webster, J.,

527 and Wilson, D. C.: Atmospheric waves and global seismoacoustic observations of the January 2022 Hunga

528 eruption, Tonga, Science (80-. )., 377, 95–100, https://doi.org/10.1126/science.abo7063, 2022.

529 Tonga Volcanic Eruption & Tsunami: https://appliedsciences.nasa.gov/what-we-do/disasters/disasters-

530 activations/tonga-volcanic-eruption-tsunami-2022, last access: 15 December 2022.

531 OCIMF: Estimating The Environmental Loads On Anchoring Systems, Oil Companies International

532 Marine Forum, London, 33 pp., 2010.

533 Oh, M. J., Ham, S. H., and Ku, N.: The coefficients of equipment number formula of ships, J. Mar. Sci.

534 Eng., 8, 1–11, https://doi.org/10.3390/jmse8110898, 2020.

535 Ohgaki, K., Yoneyama, H., Suzuki, T., and IEEE: Evaluation on safety of moored ships and mooring

536 systems for a tsunami attack, 2008.

537 Omira, R., Ramalho, R. S., Kim, J., González, P. J., Kadri, U., Miranda, J. M., Carrilho, F., and Baptista,

538 M. A.: Global Tonga tsunami explained by a fast-moving atmospheric source, Nat. 2022 6097928, 609,

539 734–740, https://doi.org/10.1038/s41586-022-04926-4, 2022.

540 Pakoksung, K., Suppasri, A., and Imamura, F.: The near-field tsunami generated by the 15 January 2022

541 eruption of the Hunga Tonga-Hunga Ha'apai volcano and its impact on Tongatapu, Tonga, Sci. Rep., 12,

542 15187, https://doi.org/10.1038/s41598-022-19486-w, 2022.

543 Pararas-Carayannis, G.: The tsunami generated from the eruption of the volcano of Santorin in the Bronze

544 Age, Nat. Hazards, 5, 115–123, https://doi.org/10.1007/BF00127000, 1992.

545 Pararas-Carayannis, G.: Volcanic tsunami generating source mechanisms in the eastern Caribbean region,

546 Sci. Tsunami Hazards, 22, 74–114, 2004.

547 Paris, R.: Source mechanisms of volcanic tsunamis, Philos. Trans. R. Soc. A Math. Phys. Eng. Sci., 373,

548 https://doi.org/10.1098/rsta.2014.0380, 2015.

549 Paris, R., Switzer, A. D., Belousova, M., Belousov, A., Ontowirjo, B., Whelley, P. L., and Ulvrova, M.:

550 Volcanic tsunami: A review of source mechanisms, past events and hazards in Southeast Asia (Indonesia,

551 Philippines, Papua New Guinea), https://doi.org/10.1007/s11069-013-0822-8, 7 January 2014.

552 Proudman, J.: The Effects on the Sea of Changes in Atmospheric Pressure., Geophys. J. Int., 2, 197–209,

553 https://doi.org/10.1111/J.1365-246X.1929.TB05408.X, 1929.

554 Rabinovich, A. B.: Spectral analysis of tsunami waves: Separation of source and topography effects, J.

555 Geophys. Res. Ocean., 102, 12663–12676, https://doi.org/10.1029/97JC00479, 1997.

556 Ramírez-Herrera, M. T., Coca, O., and Vargas-Espinosa, V.: Tsunami Effects on the Coast of Mexico by

557 the Hunga Tonga-Hunga Ha'apai Volcano Eruption, Tonga, Pure Appl. Geophys.,

558 https://doi.org/10.1007/S00024-022-03017-9, 2022.

559 Sakakibara, S., Takeda, S., Iwamoto, Y., and Kubo, M.: A hybrid potential theory for predicting the motions

560 of a moored ship induced by large-scaled tsunami, Ocean Eng., 37, 1564–1575,

561 https://doi.org/10.1016/J.OCEANENG.2010.09.005, 2010.

562 Satake, K., Rabinovich, A. B., Dominey-Howes, D., and Borrero, J. C.: Introduction to "Historical and

563 Recent Catastrophic Tsunamis in the World: Volume I. The 2011 Tohoku Tsunami,"

564    https://doi.org/10.1007/s00024-012-0615-0, 1 June 2013.

565    Shampine, L. F.: Some Practical Runge-Kutta Formulas, Math. Comput., 46, 135,
566    https://doi.org/10.2307/2008219, 1986.

567    Shevchenko, G., Shishkin, A., Bogdanov, G., and Loskutov, A.: Tsunami Measurements in Bays of
568    Shikotan Island, Pure Appl. Geophys., 168, 2011–2021, https://doi.org/10.1007/s00024-011-0284-4, 2011.

569    Shigeki, S. and Masayoshi, K.: Initial attack of large-scaled tsunami on ship motions and mooring loads,
570    Ocean Eng., 36, 145–157, https://doi.org/10.1016/j.oceaneng.2008.09.010, 2009.

571    SPDA Actualidad Ambiental: https://www.actualidadambiental.pe/derrame-petroleo-cronologia-de-lo-
572    sucedido-segun-el-capitan-del-buque-mare-doricum-video/, last access: 1 March 2024.

573    Tahar, A. and Kim, M. H.: Hull/mooring/riser coupled dynamic analysis and sensitivity study of a tanker-
574    based FPSO, https://doi.org/10.1016/j.apor.2003.02.001, 2004.

575    Terry, J. P., Goff, J., Winspear, N., Bongolan, V. P., and Fisher, S.: Tonga volcanic eruption and tsunami,
576    January 2022: globally the most significant opportunity to observe an explosive and tsunamigenic
577    submarine eruption since AD 1883 Krakatau, Geosci. Lett., 9, 24, https://doi.org/10.1186/s40562-022-
578    00232-z, 2022.

579    Thomson, R. E., Rabinovich, A. B., Fine, I. V., Sinnott, D. C., McCarthy, A., Sutherland, N. A. S., and
580    Neil, L. K.: Meteorological tsunamis on the coasts of British Columbia and Washington, Phys. Chem. Earth,
581    34, 971–988, https://doi.org/10.1016/j.pce.2009.10.003, 2009.

582    CNAT: https://www.tvperu.gob.pe/noticias/nacionales/cnat-no-existe-alerta-de-tsunami-en-el-litoral-
583    peruano, last access: 6 February 2022.

584    World Bank: https://www.worldbank.org/en/news/press-release/2022/02/14/tonga-volcanic-eruption-and-
585    tsunami-world-bank-disaster-assessment-report-estimates-damages-at-us-90m, last access: 28 February
586    2024.

587    Wilson, R., Lynett, P., Eskijian, M., Miller, K., LaDuke, Y., Curtis, E., Hornick, M., Keen, A., and Ayca,
588    A.: TSUNAMI HAZARD ANALYSIS AND PRODUCTS FOR HARBORS IN CALIFORNIA, in:
589    Tsunami Hazards: Innovations in Mapping, Modeling, and Outreach, https://doi.org/10.1130/abs/2017am-
590    306344, 2017.

591    Wright, C. J., Hindley, N. P., Alexander, M. J., Barlow, M., Hoffmann, L., Mitchell, C. N., Prata, F.,
592    Bouillon, M., Carstens, J., Clerbaux, C., Osprey, S. M., Powell, N., Randall, C. E., and Yue, J.: Surface-to-
593    space atmospheric waves from Hunga Tonga–Hunga Ha'apai eruption, Nature, 609, 741–746,
594    https://doi.org/10.1038/s41586-022-05012-5, 2022.

595    Xu, Z., Sun, L., Rahman, M. N. A., Liang, S., Shi, J., and Li, H.: Insights on the small tsunami from January
596    28, 2020, Caribbean Sea MW7.7 earthquake by numerical simulation and spectral analysis, Nat. Hazards,
597    111, 2703–2719, https://doi.org/10.1007/s11069-021-05154-1, 2022.

598    Yokoyama, I.: A geophysical interpretation of the 1883 Krakatau eruption, J. Volcanol. Geotherm. Res., 9,
599    359–378, https://doi.org/10.1016/0377-0273(81)90044-5, 1981.

600    Zheng, Z., Ma, X., Yan, M., Ma, Y., and Dong, G.: Hydrodynamic response of moored ships to seismic-
601    induced harbor oscillations, Coast. Eng., 176, 104147, https://doi.org/10.1016/j.coastaleng.2022.104147,
602    2022.

603